The Astrophysical Journal, 715:468–476, 2010 May 20 doi:10.1088/0004-637X/715/1/468

THE CORONAL AND HELIOSPHERIC 2007 MAY 19 EVENT: CORONAL MASS EJECTION, EXTREME ULTRAVIOLET IMAGER WAVE, RADIO BURSTS, AND ENERGETIC ELECTRONS

A. Kerdraon[1], M. Pick[1], S. Hoang[1], Y.-M. Wang[2], and D. Haggerty[3]
[1] LESIA, UMR CNRS 8109, Observatoire de Paris, Meudon 92195, France
[2] Space Science Division, Naval Research Laboratory, Washington, DC 20375-5352, USA
[3] Johns Hopkins University, Applied Physics Laboratory, Laurel, Maryland, USA
Received 2010 February 8; accepted 2010 March 31; published 2010 April 29

ABSTRACT

We study the global development of the 2007 May 19 event and investigate the origin and the escape of the energetic electrons responsible for the interplanetary bursts and for the solar energetic particle event. The data analysis combines radio spectral and imaging observations with *STEREO* EUV observations. We also use the direction-finding capabilities on the *Wind*/Waves radio instrument. Electron acceleration and injections into the interplanetary medium occur with some delay after the flare. It is shown that they are related to the expansion of the coronal mass ejection and of the extreme ultraviolet imager wave. There are two accelerations at two different locations in the corona which correspond to two different electron trajectories in the interplanetary medium.

Key words: solar–terrestrial relations – Sun: coronal mass ejections (CMEs) – Sun: particle emission – Sun: radio radiation

1. INTRODUCTION

In the past decade, much insight has been gained from multi-wavelength observations into the initiation and development of coronal mass ejections (CMEs), of their link with the structure and dynamics of the surrounding corona, and of their association with other phenomena such as solar energetic particle (SEP) events. CME development in the corona is associated with large-scale transient coronal waves well observed in extreme ultraviolet imager (EUV) imaging telescopes (Thompson et al. 1999; Biesecker et al. 2002). EUV waves appear as a bright front that propagates across the solar disk. An expanding dimming appears behind the wave as a consequence of the opening in the corona of the magnetic field during the CME development; the EUV waves onsets are associated with the CME-expanding loops (e.g., Attrill et al. 2007; Patsourakos et al. 2009). A large amount of magnetic energy, responsible for particle acceleration, is released during eruptive phenomena that include flares, eruptive prominences, CMEs, and shocks. Thus nonthermal radio spectral and imaging observations, though restricted to investigations of energetic electrons, have provided important diagnostics on such problems as:

1. Where does magnetic reconnections occur between the expanding CME and the surrounding environment? Joint coronagraph, EUV, and radio imaging observations showed that the CMEs develop at large scale by successive reconnections with the surrounding magnetic structures (Mandrini et al. 2007; Pick & Vilmer 2008). When observed near the limb, the radio sources trace the CME opening (Pick et al. 1998). When observed above the solar disk, their angular extent is comparable with the extent of the EUV waves or Moreton waves (Pohjolainen et al. 2001; Pick et al. 2005).
2. When and where are the coronal shocks associated with CMEs produced? Compression waves or shocks were revealed by white light coronagraphs (Vourlidas et al. 2003) and also by radio type II burst observations (Lario & Pick 2008). They can be formed at the flanks of CMEs during their lateral expansion. This lateral expansion creates a compression region between closed and open field lines near which groups of type III radio bursts were detected (e.g., Yan et al. 2006).
3. What is the association between flares and CMEs with SEP events? There have been several conflicting results on the origin of the energetic electrons detected in situ and on their association with flares and CMEs. Krucker et al. (1999) and Haggerty & Roelof (2002) identified two kinds of impulsive electron events at energies above 13 keV: (1) events initiated at the onset of a radio type III burst, which suggests that these electrons are part of the population producing the type III burst emission and (2) events in which the electrons are released up to half an hour later than the onset of type III bursts. Several explanations have been proposed for these delayed events: CME-driven shocks (Simnett et al. 2002), acceleration by large-scale coronal perturbation associated with coronal EUV or Moreton waves (Krucker et al. 1999), and in the wake of the associated CME (Maia & Pick 2004). Maia and Pick argued that the regions of magnetic field interaction, which are identified in the corona by their radio emissions, are the regions of secondary acceleration of energetic electrons responsible for delayed electron events. We note that the discrepancy between these different approaches could be partly explained by the fact that, most often, the radio data analysis in previous studies has been restricted to the temporal association and did not include the localization of the radio sources.

The aim of this paper is to study the large-scale development of an event that was observed above the solar disk and to investigate the origin and the escape of the energetic electrons responsible for the interplanetary radio bursts and for the SEP event. The data analysis combines radio spectral and imaging observations with *STEREO* EUV observations. By comparing with previous studies on similar topics, the present study takes advantage of the new capabilities of the EUVI with a cadence of 2.5 minutes at 171 Å (Howard et al. 2008); moreover, the direction-finding capabilities on the *Wind*/Waves radio instrument are used to determine the elevation and azimuth of the radio emissions in interplanetary space (Hoang et al. 1998).

The active region (AR) 10956 generated a B9.5 X-ray flare on 2007 May 19 starting at 12:50 UT with a first and highest

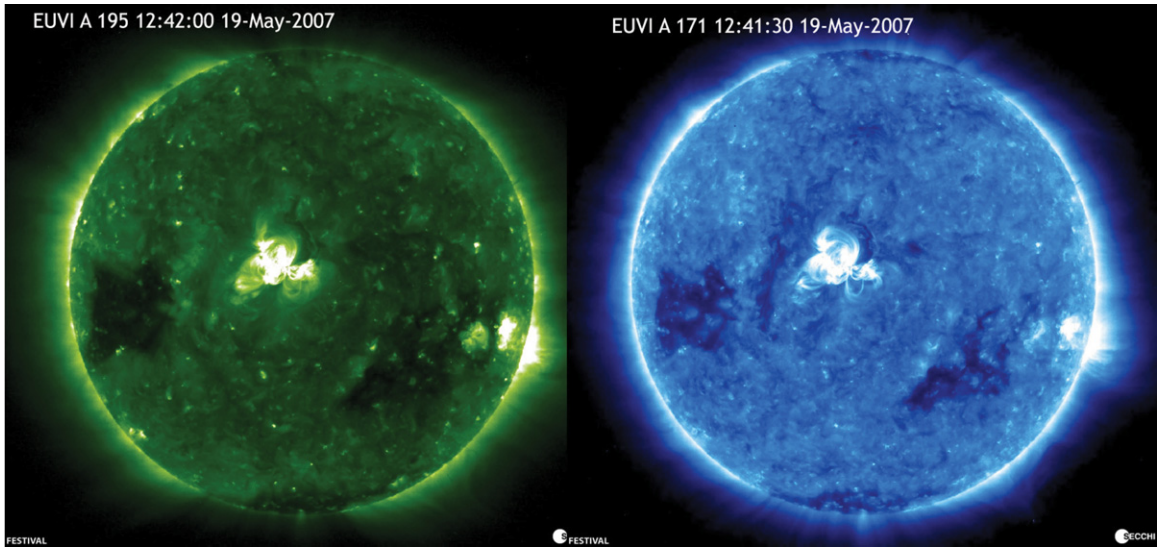

Figure 1. *STEREO-A*/EUVI images of the corona at 195 Å(left) and at 171 Å (right) on 2007 May 19.

flux peak at 12:51:50 UT. This flare was accompanied by a filament eruption, post-eruption flare loops, an EUV dimming, a coronal wave, a faint multi-front CME, and complex radio emissions. This event, observed by the *Solar TErrestrial RElations Observatory* (*STEREO*), stimulated several studies of the filament eruption (Liewer et al. 2009; Bone et al. 2009), of the solar magnetic field and coronal dynamics of the eruption in the framework of CME initiation mechanisms (Li et al. 2008), and of the EUV coronal wave (Veronig et al. 2008). The associated complex radio burst lasted for more than 30 min and was accompanied by an SEP event. The twin *STEREO* spacecraft *A* and *B* were respectively 5.°6 ahead and −2.°8 behind from the Earth; this weak angular separation is a favorable situation for comparison between *STEREO* and ground based observations. A radio spectrogram which covers a broad frequency range from 459 MHz to 30 KHz was constructed by combining data obtained with different radio spectrographs: ARTEMIS 459–200 MHz (Kontogeorgos et al. 2006), San Vito 85–70 MHz (http://www.ngdc.noaa.gov/stp/SOLAR/ftpsolarradio.html), Nançay-DAM 70–15 MHz (Lecacheux 2000), and *Wind*/Waves 14 MHz–30 kHz (Bougeret et al. 1995). The Multifrequency Nançay Radioheliograph (NRH) provided images at five frequencies from 432 to 150 MHz (Kerdraon & Delouis 1997).

2. DATA ANALYSIS

Figure 1 shows an EUVI image from *STEREO A* observed at 195 Å and 171 Å before the flare/CME event. The overall coronal structure is rather simple: the image essentially shows the AR responsible for the flare and two broad coronal holes located, respectively, east and west of the AR.

A coronal wave is observed by the two *STEREO* spacecraft at both 171 Å and 195 Å. It starts at ∼12:51 UT and was studied in detail by Veronig et al. (2008). We have reproduced in Figure 2 (right lower panel) one of their figures that shows the dynamical behavior of this wave. In this figure, the solid lines mark the wave fronts identified at 171 Å (white) and 195 Å (black). The dashed lines indicate the circular fits to the three earliest wave fronts. The wave is expanding very clearly westward and then northward, after 12:56:30 UT. It is more difficult to see this wave on the east side of the AR. There are only low contrast indications of its presence on the 195 Å

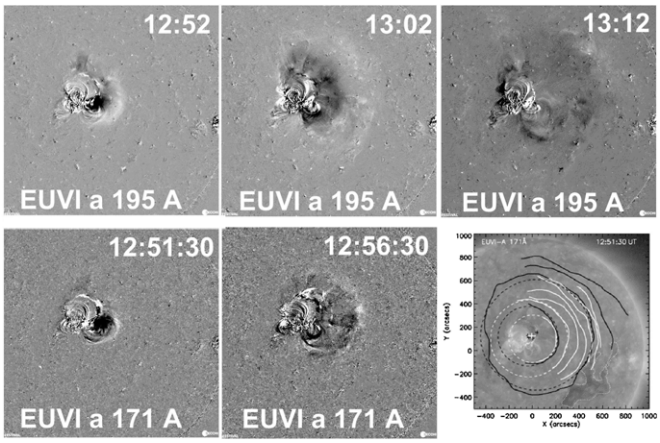

Figure 2. Combined *STEREO-A*/EUVI images at 195 Å (top) and 171 Å (bottom) on 2007 May 19 that illustrate the progression of the EUV wave. The lower right-hand panel from Veronig et al. (2008) displays the wave front segments (solid lines) identified at 171 Å (white) and 195 Å (black). The dashed lines indicate circular fits.

EUVI running differences. Veronig et al. (2008) argued that the AR region may represent an obstruction for the eastward propagation of the wave.

Two CMEs were reported for this period in the SOHO catalog: the first one, CME1, was observed at a position angle of 260° with a mean speed of 960 km s^{-1} and the second one, CME2, at 310° with a speed of 290 km s^{-1}.

The upper part of Figure 3 shows a 0.4–300 MHz dynamic radio spectrum of this event. The flux measured at 150 MHz by the NRH is plotted as a function of time in the lower panel. The decametric spectrum shows a coronal type II burst which is not detected at WAVES. The burst started at 12:50:10 UT at 80 MHz (fundamental emission) exhibiting three spectral lanes which correspond, respectively, to the fundamental, the second, and the third harmonic emission. The second harmonic emission is well observed by the NRH at 150 MHz from 12:52:20 UT to 12:54:00 UT which is indicated in red in the NRH flux plot. The onset of this type II burst is followed by three successive episodes of interplanetary type III bursts.

1. The first one (∼12:53:43 UT) corresponds to a single weak type III burst which is not detected in the spectra

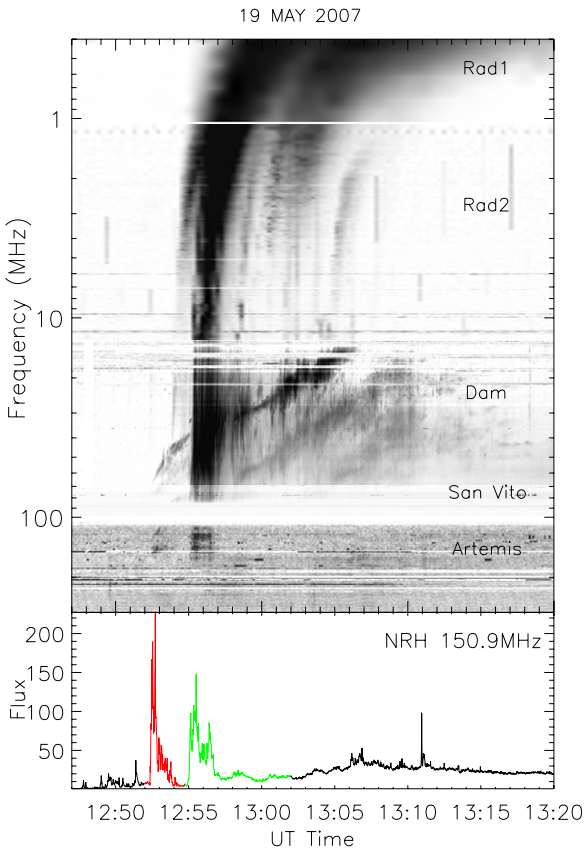

Figure 3. Dynamic radio spectrum in the frequency range 0.4–300 MHz. The flux vs. time measured at 150 MHz by the NRH is reported in the lower panel. The type II and type III bursts are shown by red and green colors, respectively.

at metric wavelengths but well observed at 150 MHz by the NRH.

2. The second one (∼12:55 UT to 12:57 UT) is a bright group of bursts starting low in the corona at 250 MHz (see the NRH 150 MHz flux indicated in green in Figure 3) and extending in the interplanetary medium at frequencies lower than 400 kHz.
3. The third group (∼12:58 UT to 13:02 UT) consists of type III bursts starting much higher in the corona around roughly 20 MHz. On the *Wind*/Waves spectrum, they merge with the second group at low frequencies. With the spectral information alone, it is difficult to say if they are related to the type II burst which is present at the same time. We can only state that the type II fundamental emission frequency is close to the type III starting frequency. However, as the type III burst emission at frequencies around 20 MHz is unpolarized, these bursts are produced more likely at the second harmonic of the plasma frequency and should be emitted at higher altitude than the type II burst.

2.1. Joint EUV and Radio Data Analysis

The onset of the coronal wave and of the type II burst was preceded by a period of weak radio activity.

1. Prior to the flare onset at 12:48 UT, two radio sources were detected; their locations are superimposed on an Hα image shown in Figure 4, left panel. The southern source is sporadic and was observed after 08:00 UT (the observing onset time of the NRH), at 150 and 236 MHz. The northern source appeared at 236 MHz for a few seconds at 12:43:11 UT.
2. After the flare onset, weak bursts were detected at 236 MHz from 12:50 to 12:52:30 UT. Their emitting sources lie above the filament and drift from its northern edge to its southern edge (see Figure 4, right panel).
3. The end of this period is marked by a sudden development of the eruptive event; it is characterized by a rapid rise of the filament and of a bunch of arches to the southwest of the AR, as shown in Figure 5 (left panel). This coincides with the first observation of the coronal wave at 12:51:30 UT and with the onset of the type II burst.
4. In Figure 5 (right panel), the positions at 150 MHz of the type II burst measured at 12:52:43 and 12:53:28 UT are marked on the *STEREO-B* EUVI image at 12:52:18 UT. This coronal type II burst appears to propagate in the west–northwest direction. In the left panel, the type III burst sources of the single event (green) and of the first bright group near its beginning and end (blue and red) are marked on the *STEREO-A* image at 12:51:30 UT. These images as well as the images shown in Figures 6 and 7 have been corrected for the angle between the Earth and *STEREO A* and *B*.

In Figure 6, the source of the first single type III burst at 12:53:40 UT is overlaid (green color) on a running difference image of *STEREO-A* EUVI taken at 12:54:00 UT. In Figure 7, two running difference images of *STEREO-B* EUVI are shown at two successive times just prior and after the occurrence of the first group of type III bursts. The burst sources observed at two different times are overlaid on these images (blue and red colors). These two figures show that the sources of these bursts, at 150 MHz, coincide spatially with the bright front edge of the coronal wave. The start velocity of the coronal wave measured with a cadence of 2.5 min was 460 km s^{-1}.

2.2. Localization of the Interplanetary Radio Bursts

We use the direction-finding capabilities (Manning & Fainberg 1980) of the *Wind*/Waves receiver to derive the direction of the radio bursts. Results are shown at 428 kHz in Figure 8. The intensity–time profile (upper panel) shows two peaks, which correspond to the two intense type III groups in the meter-decameter wavelength range. The derived radio source azimuth, as viewed from *Wind*, is plotted (middle panel) with positive values for a source coming from the east of the *Wind*–Sun line, and negative values for the west side. The bottom panel displays the radio source elevation angle measured from the ecliptic plane, with positive values for north directions. From the azimuth and elevation plots, the radio emission at the first peak comes nearly from the Sun–*Wind* direction. This direction is confirmed to be steady by direction finding performed at lower frequencies and is compatible with the positions observed between 12:52 and 12:57 UT at 150 MHz. The second peak is clearly observed in a different direction (5° east, 5° north) and is also found to have a stable direction at lower frequencies. This suggests a different origin of the second group of type III bursts. We note that the onset of this second group at 12:58 UT coincides approximately with the time when the coronal wave is expanding very clearly in the north of the AR and stops its expansion toward east, when observed at 171 Å. To deduce the distance of the emissions source at the first peak intensity at 428 kHz, we use the direction measured by *Wind* together with the difference of the onset times observed by the *Wind* and *Ulysses* spacecraft (Hoang et al. 1998). The triangulation analysis results in a distance of 0.15 AU from the sun center. Reiner et al. (2009) found a heliocentric distance of 0.2 AU for the same radio burst at

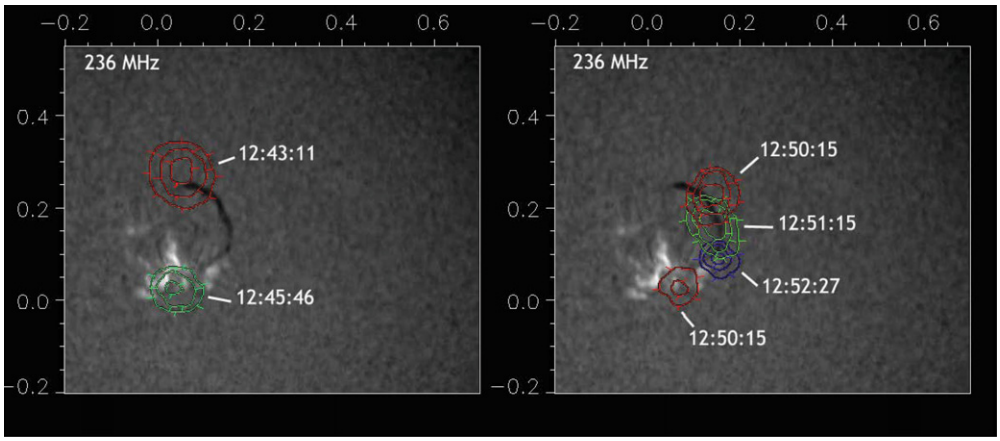

Figure 4. Radio sources are overplotted on an Hα image from Kanzelhoehe Observatory. The image was obtained at 08:04:31 UT and then rotated westward by 2°. Left panel: sources observed prior to the flare. Right panel: sources observed after the flare occurrence during the pre-eruptive period.

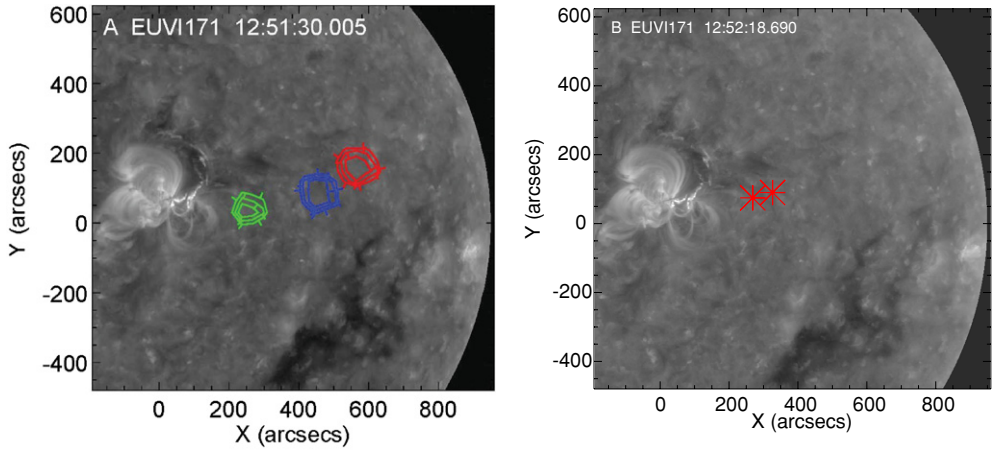

Figure 5. Radio sources observed at 150 MHz are overplotted on an *STEREO-A* or B EUV image at 171 Å. Left panel: source of the first single type III (green color) and sources (blue and red colors) during the first metric type III group. Right panel: source of the second harmonic of the type II burst measured at two different times (see Figure 3).

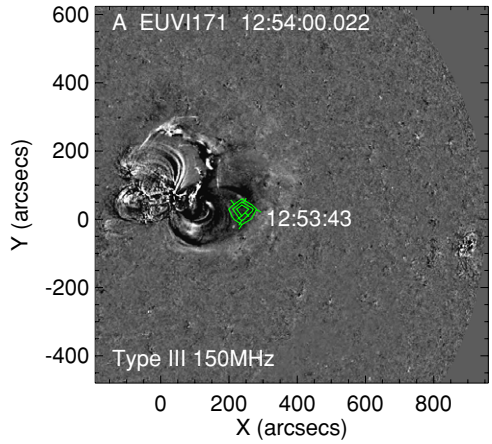

Figure 6. Source (green color) of the single type III burst at 12:53:43 UT is overplotted on the (closest) in time *STEREO-A*/EUVI image at 12:54:00 UT.

425 kHz, using a different technique based on direction finding by the *Wind* and *STEREO* radio experiments.

2.3. The SEP Event

The 2007 May 19 flare/CME was associated with a rather weak SEP event which was identified by the instruments on board *ACE* and *STEREO A* and *B* (Mewaldt et al. 2008; Bučík et al. 2009). The protons were detected in the low energy range 6–10 MeV. In contrast, the electron event was quite strong; it was detected in the four energy channels of the ACE/EPAM in the energy range 38–315 keV (Gold et al. 1998). Figure 9 displays for each channel the 10 minute averaged data. There is no apparent velocity dispersion between the lowest and highest energy channels, which means that the probe entered in a region already filled with energetic particles. Therefore, the probe did not observe the beginning of the event. The pitch angle distributions, not reproduced here, clearly show that the event is almost completely isotropic. This event starts to be detected at 13:30 ± 10:00 UT which leads to an inferred electron release time before 13:05:00 ± 10:00 UT (corrected by 500 s to account for the photon travel time).

3. SUMMARY AND DISCUSSION

The main points of the data analysis can be summarized as follows:

1. *Initiation of the eruptive event*
   Following the flare occurrence and during the pre-eruptive period, radio sources were detected above the filament. These sources which are from nonthermal origin are very likely due to magnetic field line interaction; they are

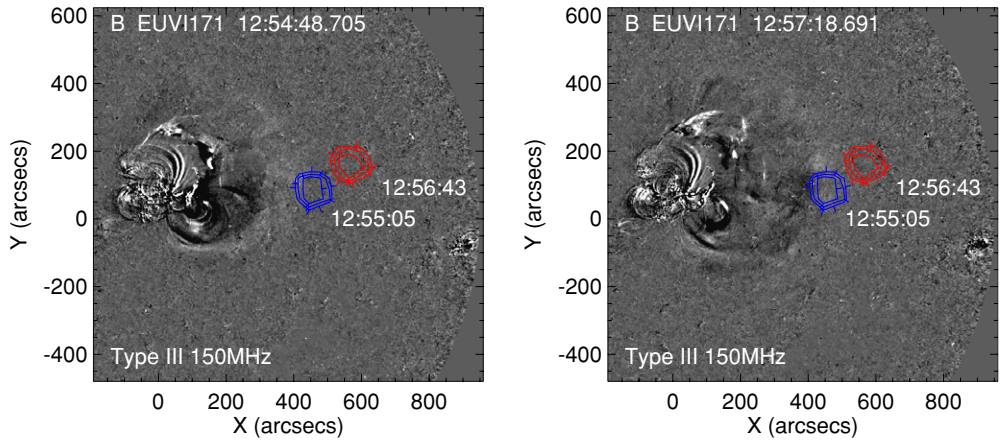

Figure 7. Running difference images of *STEREO-B*/EUVI are shown just prior to and after the occurrence of the first group of type III bursts (see the text). The source of these bursts observed at two different times (blue and red) are overplotted on the images.

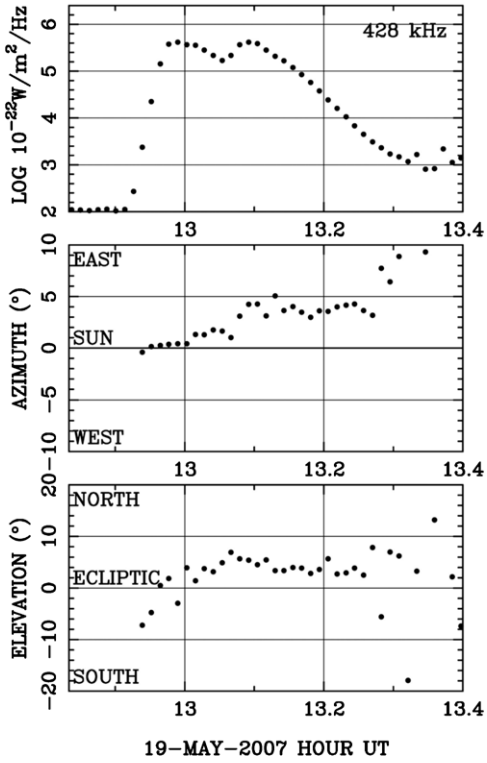

Figure 8. *Wind*/Waves direction determination for the 2007 May 19 event. The plots show the flux density, azimuth, and elevation of the radio source at 428 kHz. Two successive but overlapping sources are seen, the second one being directed to the east and north of the first one.

first detected at the northern edge of the filament, then drift along the filament in projection. At the end these sources are located near the region from which the fast expanding arches originate, the coronal wave and the shock which is traced out by the type II radio burst. These observations are confronted to the model proposed by Li et al. (2008). The authors discussed in detail the onset and evolution of this event in the context of current models of CME initiation. They estimated the coronal magnetic fields using a Potential Field Source Surface (PFSS) model based on the daily updated Michelson doppler imager synoptic map. Figure 10 (Figures 4(b) and (d) in their paper) displays PFSS field lines (left panel) originating from the AR (right panel) and the overlying multi-flux systems. Flux systems are color coded (for details, see their paper) as dark blue, green, and light blue. The purple lines mark the separation between the flux systems and the (yellow) large-scale overlying streamer. The authors suggested that this multi-flux topology may correspond to a lateral magnetic break out eruption, where reconnection at the coronal null point between the two side lobes (dark blue and light blue) transfers the restraining flux (light blue) overlying the filament to the central (green) and streamers (yellow) flux systems. This lateral reconnection reduces the restraining force on the filament, thus leading to a runaway destabilization of the system. In the present study, the detection of successive radio sources, first above the north edge of the filament and then drifting toward the south, is compatible with the model in which the magnetic reconnection will start at the coronal null point and then will trigger the nonthermal particles observed by the radio emission. This observation is also compatible with the idea that successive magnetic reconnections will contribute to reduce the restraining force on the filament. However, although we may have evidence of magnetic reconnections above the filament in the null point region, we cannot say that these reconnections are the only cause of the filament eruption. Alternatively, the eruption may be due to magnetic field modifications (such as flux cancellation) below the filament, and the reconnections at higher altitudes a result from them.

2. *Origin of the coronal type II radio burst*

   The coronal wave is first detected south of the AR (see Figure 2) surrounding the EUV loops (see Figure 5), then expands rapidly northward above the filament. In agreement with previous studies, we interpret the occurrence of the coronal type II burst as a consequence of this rapid expansion of the coronal wave and the build-up of a compression region of higher density than the medium surrounding the EUV wave (e.g., Pohjolainen et al. 2001; Vršnak et al. 2005) and the associated CME flank (see Vourlidas et al. 2003; Yan et al. 2006). We note that compared to the EUV wave, the coronal type II radio emission is a much more localized phenomenon.

3. *Origin and propagation of the electron beams producing the interplanetary type III radio bursts*

   As the coronal wave expands and the associated CME moves up in the corona, it is expected that they will

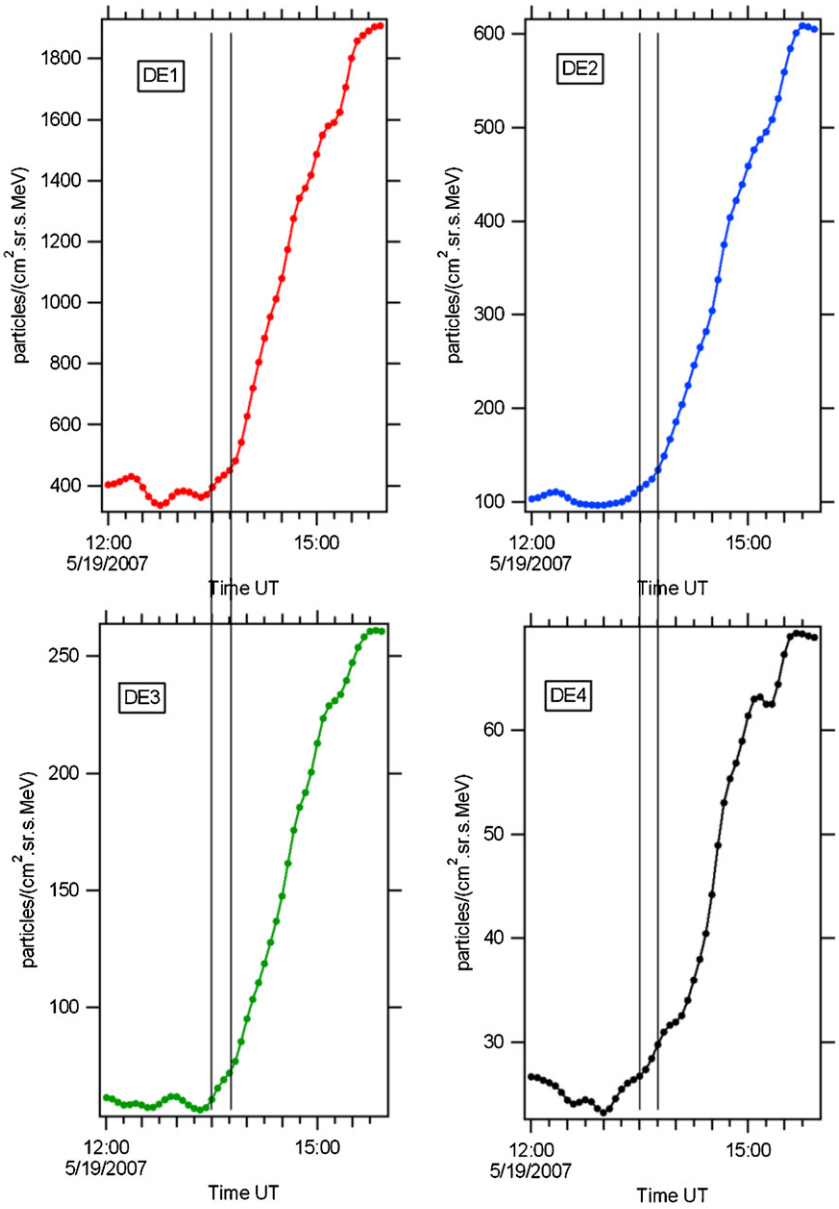

Figure 9. Near relativistic electron event observed on 2007 May 19 at 1 AU by ACE/EPAM in four energy channels in the range 38–315 keV (DE1–DE4). There is no apparent velocity dispersion between the lowest and highest energy channels.

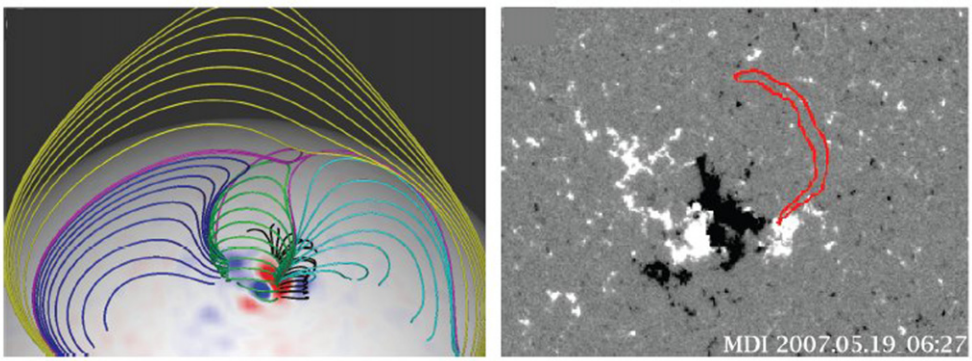

Figure 10. Left panel: PFSS field lines originating from AR 10956. The black arcade overlies the neutral line associated with the filament. Flux systems are color coded as green (central arcade), dark blue (east arcade), light blue (west arcade overlying black arcade), and yellow (large-scale overlying streamer belt arcade). The purple lines mark topological separation between the flux systems. Right panel: the outline of the Hα filament is overplotted on the magnetogram at 6:27 UT (from Li et al. 2008, see their Figure 4).

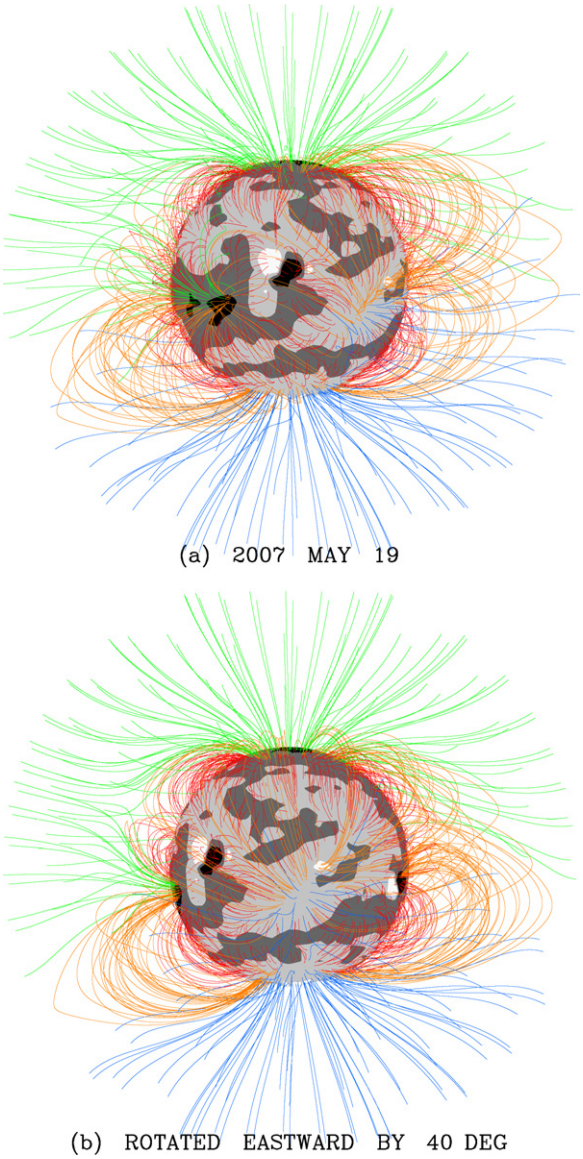

Figure 11. (a) Magnetic field configuration. The corona field is seen by PFSS extrapolation of Mount Wilson Observatory photospheric field map for CR 2056. (b) The same image has been rotated east by 40°.

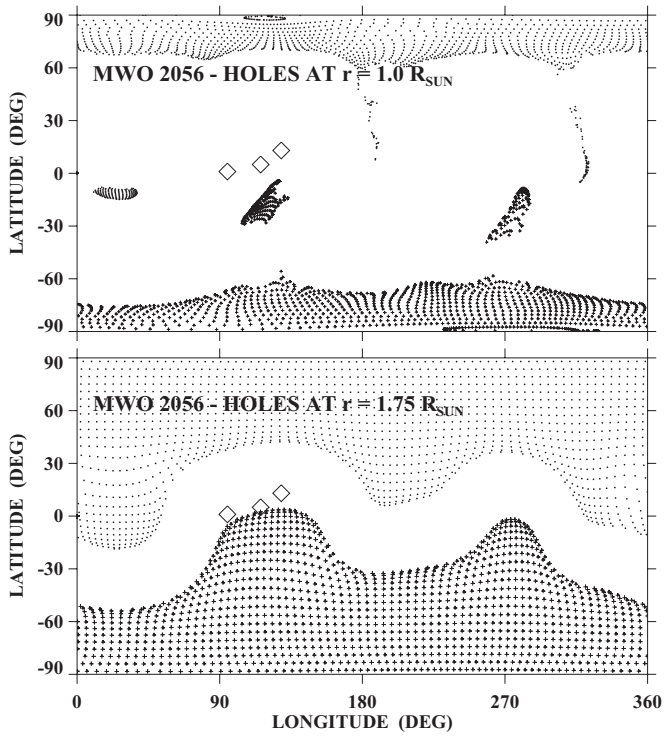

Figure 12. CR 2056 map. Upper panel: the open photospheric field lines region above the coronal holes. Lower panel: the coronal hole open field lines extension above the coronal hole, at an altitude of 0.75 $R_\odot$ above the solar disk. The positions of the type III burst sources (diamonds) have been reported on the CR map. The central meridian corresponds to a Carrington longitude at 72°.

interact with the surrounding magnetic structures. The occurrence of the two successive groups of kilometric interplanetary (IP) type III bursts provides evidence of successive interactions between closed and open field lines. The emitting sources of the single type III burst and of the first group coincide spatially with the front of the coronal EUV wave; they are detected, respectively, at 150 MHz and 250 MHz hence in the corona typically at an altitude of the order 0.3–1.0 $R_\odot$ above the photosphere. These observations are consistent with an origin of the radio-emitting electron beams in the interaction between closed and open field lines. This is in agreement with previous results (e.g., Yan et al. 2006). If it is assumed that the second harmonic of type III bursts is emitted in the ordinary mode, the polarization measurements from the NRH and the DAM spectrograph show that the electron beams propagate outward along magnetic field lines corresponding to a south polarity. Figure 1 shows the presence of a large coronal hole in the western hemisphere. Figure 11 (upper panel) displays a PFSS extrapolation of the photospheric field out to a source surface at 2.5 $R_\odot$ (Wang & Sheeley 1992). In the lower panel, the image has been rotated east by 40°. The open field lines emerging from the large coronal hole are widely diverging. This strongly suggests that the electron beams producing IP type III bursts are injected and propagate along these field lines. The sign of the polarization of these bursts is compatible with the inward solar direction of the field lines (blue color in Figure 11).

From the same PFSS model, we made a comparison between the positions of the open field lines emerging from the western coronal hole and the positions of the type III radio burst at 150.9 MHz between 12:55 and 12:57 UT. The field lines reach the radio positions at an altitude of 1.75 $R_\odot$. Figure 12 shows the result in a synoptic Carrington representation. The upper panel displays the distribution of open field line regions at the photosphere. The lower panel displays the extension of this region at an altitude of 1.75 $R_\odot$. The positions of the sources of type III bursts are marked in the same map. They lie close to or in the open magnetic field region. If we assume that the type III radio emission is produced at the second harmonic of the plasma frequency, the electron density at 1.75 $R_\odot$ will be of the order of 8 times the density of the Saito model (Saito et al. 1977). This value is consistent with the fact that the plasma, in the regions where are produced the type III radio bursts, is indeed compressed as the result of the CME expansion (Yan et al. 2006; Cohen et al. 2009). It is noteworthy that the heliocentric distance of 0.15 AU found for the first type III bursts group at 428 kHz (see Section 2.2) implies a density of 2.26×10^3 cm^{-3}, assuming that the interplanetary radio burst is emitted at the fundamental

frequency. This density value is found to be 3.8 times the density model of Leblanc (Leblanc et al. 1998) corrected for the actual density measured at 1 AU at the time of the observation. This overdensity at 0.15 AU is lower than the one observed at 1.75 $R_{\odot}$, consistent with the fact that the altitude of the CME is much lower than 0.15 AU at the time of the radio emission at 428 kHz. The second group of type III radio bursts starts at lower frequencies, below 40 MHz. In contrast to the first group, the polarization is too weak to be measured at decametric wavelengths. The onset time coincides approximately with the moment when the northern edge of the coronal wave has reached its maximum latitude. *Wind*/Waves measurements show that their locations at 428 kHz are 5°N of the ecliptic plane and 5°E of the Sun–*Wind* line. The type III electrons may be accelerated in the north of the AR, in the high corona, and injected along open magnetic field lines belonging to the green magnetic flux system (see Figure 11)

4. *The SEP event*
The electron event is quite strong; it was detected in the highest energy channel of the ACE/EPAM experiment. Initially, this event was not magnetically connected with the probe and the inferred release time for the electrons, <13:05:00 ± 10:00 UT, cannot be determined with accuracy. Krucker et al. (1999) suggested that at least some impulsive electron events at energy greater than 25 keV and not associated in time with metric type III bursts are more likely related to a propagating Moreton or EUV wave than to the flare itself. For events which present a large discrepancy between the flare location and the region which is assumed to be connected to the Earth, they concluded that the wave was too slow to arrive in time at the magnetically connected point. The present study shows that the region of electron release is not only dependent on the wave propagation but also strongly on (1) the geometry of the open magnetic field lines which will connect the source of electrons with the spacecraft and (2) the altitude, where the electrons are released, which is likely higher than the EUV wave front altitude, the source of electrons being located along or near the edge of the CME. Krucker also noted that the EUV waves are faster at higher altitudes.

Finally, if we assume that the SEP electrons are the ones at the origin of the interplanetary type III radio bursts, we can draw conclusions on their origin; for the first group of interplanetary bursts, the observations are in favor of a reconnection process between the CME expanding loops and the open magnetic field lines emerging from the coronal hole. The coronal shock is outlined by its type II radio emission; as this emission frequency is much lower than the starting frequency of the emission of the electrons beams, this shock is clearly too high in the corona to be at the origin of the acceleration of the electrons responsible for the radio type III bursts. The conclusion is less clear for the second group of type III radio bursts: coronal shock or reconnection? The argument in favor of reconnection mechanism is that the radio emission of the electrons beams originates from a region northeast of the AR, and that the shock travels toward the west of the AR.

4. CONCLUSION

From the study of the 2007 May 19 event, we have derived new insight about the flare/eruption development and the electron injection in the IP medium:

1. This event consists in a compact flare, with almost no radio counterparts, followed by a filament eruption, two CMEs, an EUV wave, and radio emissions associated with a shock wave and electron beams. It has an unusual radio spectrum, mainly because the shock related type II radio emission precedes the type III radio emission generated by electron beams.
2. Radio emission shows evidence of magnetic reconnection above the filament at the early stage of its eruption. But, we are still unable to say whether the eruption was caused by magnetic reconnections at a null point above the filament or by magnetic field modification below it.
3. The shock wave detected by its radio emission is related to the lateral expansion of the CME in the low corona and moves in the initial direction of the EUV wave.
4. Massive electron accelerations and injections in the IP medium occur with some delay after the flare. They are related to the expansion of the CME and of the EUV wave. We emphasize that there are two accelerations at two different locations in the corona, far from the flare region, which correspond to two different electron trajectories in the IP medium.

Our results, which exploit high time resolution images in the corona and direction finding in the IP medium, illustrate why it is not easy to draw conclusions on SEP origin from statistical studies mainly based on flare location and low-frequency radio spectra.

We are grateful to Anne Bouteille for her help for the figures. We thank the *STEREO* consortium who contributed to making *STEREO*, SECCHI, and S/WAVES a success. We also thank the referee for helpful comments. This work was supported by both CNES and CNRS.

REFERENCES

Attrill, G., Harra, L. K., van Driel-Gesztelyi, L., Demoulin, P., & Wuelser, J. 2007, BAAS, 38, 141
Biesecker, D. A., Myers, D. C., Thompson, B. J., Hammer, D. M., & Vourlidas, A. 2002, ApJ, 569, 1009
Bone, L. A., van Driel-Gesztelyi, L., Culhane, J. L., Aulanier, G., & Liewer, P. 2009, Sol. Phys., 259, 31
Bougeret, J.-L., et al. 1995, Space Sci. Rev., 71, 231
Bučík, R., Mall, U., Gómez-Herrero, R., Korth, A., & Mason, G. M. 2009, Sol. Phys., 259, 361
Cohen, O., Attrill, G. D. R., Manchester, W. B., & Wills-Davey, M. J. 2009, ApJ, 705, 587
Gold, R. E., et al. 1998, Space Sci. Rev., 86, 541
Haggerty, D. K., & Roelof, E. C. 2002, ApJ, 579, 841
Hoang, S., Maksimovic, M., Bougeret, J.-L., Reiner, M. J., & Kaiser, M. L. 1998, Geophys. Res. Lett., 25, 2497
Howard, R. A., et al. 2008, Space Sci. Rev., 136, 67
Kerdraon, A., & Delouis, J.-M. 1997, Coronal Phys. Radio Space Obs., 483, 192
Kontogeorgos, A., et al. 2006, Exp. Astron., 21, 41
Krucker, S., Larson, D. E., Lin, R. P., & Thompson, B. J. 1999, ApJ, 519, 864
Lario, D., & Pick, M. 2008, in The Heliosphere through the Solar Activity Cycle, ed. A. Balogh, L. J. Lanzerotti, & S. T. Suess (New York: Springer)
Leblanc, Y., Dulk, G. A., & Bougeret, J.-L. 1998, Sol. Phys., 183, 165
Lecacheux, A. 2000, in AGU Chapman Conf. Ser. 119, Radio Astronomy at Long Wavelengths, ed. R. G. Stone, K. W. Weiler, M. L. Goldstein, & J.-L. Bougeret (Washington, DC: AGU), 321
Li, Y., Lynch, B. J., Stenborg, G., Luhmann, J. G., Huttunen, K. E. J., Welsch, B. T., Liewer, P. C., & Vourlidas, A. 2008, ApJ, 681, L37
Liewer, P. C., de Jong, E. M., Hall, J. R., Howard, R. A., Thompson, W. T., Culhane, J. L., Bone, L., & van Driel-Gesztelyi, L. 2009, Sol. Phys., 256, 57
Maia, D. J. F., & Pick, M. 2004, ApJ, 609, 1082
Mandrini, C. H., Nakwacki, M. S., Attrill, G., van Driel-Gesztelyi, L., Démoulin, P., Dasso, S., & Elliott, H. 2007, Sol. Phys., 244, 25

Manning, R., & Fainberg, J. 1980, Space Sci. Instrum., 5, 161
Mewaldt, R. A., et al. 2008, 37th COSPAR Sci. Assem., 37, 2022
Patsourakos, S., Vourlidas, A., Wang, Y. M., Stenborg, G., & Thernisien, A. 2009, Sol. Phys., 259, 49
Pick, M., Malherbe, J.-M., Kerdraon, A., & Maia, D. J. F. 2005, ApJ, 631, L97
Pick, M., & Vilmer, N. 2008, A&ARv, 16, 1
Pick, M., et al. 1998, Sol. Phys., 181, 455
Pohjolainen, S., et al. 2001, ApJ, 556, 421
Reiner, M. J., et al. 2009, Sol. Phys., 259, 255
Saito, K., Poland, A. I., & Munro, R. H. 1977, Sol. Phys., 55, 121
Simnett, G. M., Roelof, E. C., & Haggerty, D. K. 2002, ApJ, 579, 854
Thompson, B. J., et al. 1999, ApJ, 517, L151
Veronig, A. M., Temmer, M., & Vršnak, B. 2008, ApJ, 681, L113
Vourlidas, A., Wu, S. T., Wang, A. H., Subramanian, P., & Howard, R. A. 2003, ApJ, 598, 1392
Vršnak, B., Magdalenić, J., Temmer, M., Veronig, A., Warmuth, A., Mann, G., Aurass, H., & Otruba, W. 2005, ApJ, 625, L67
Wang, Y.-M., & Sheeley, N. R., Jr. 1992, ApJ, 392, 310
Yan, Y., Pick, M., Wang, M., Krucker, S., & Vourlidas, A. 2006, Sol. Phys., 239, 277